MACHINE LEARNING FOR INTELLIGENT BEAM DIVERGENCE COMPENSATION IN ORBITAL ANGULAR MOMENTUM-BASED WIRELESS COMMUNICATION SYSTEMS

Md. Asif Hossain*

Department of Electrical and Electronic Engineering, Southeast University,
Dhaka, Bangladesh.

Emails: asif.hossain@seu.edu.bd (Corresponding author*)

ABSTRACT

Orbital Angular Momentum (OAM) multiplexing enables high spectral efficiency but suffers from severe signal degradation due to beam divergence. Traditional compensation methods are computationally intensive and slow, making them unsuitable for real-time use. This paper proposes a machine learning-based solution using a Deep Neural Network (DNN) that learns to predict optimal beamforming weights directly from environmental factors like distance and turbulence. Trained on diverse channel data, the model achieves 96.2% of the optimal received power while reducing latency from 100 ms to just 0.5 ms—a 200× improvement. It generalizes well to unseen scenarios, including mobile users and hardware impairments, outperforming conventional and adaptive baselines. Hardware-aware simulations confirm less than 5% performance degradation under realistic impairments, establishing a clear path to experimental validation. This work demonstrates a viable path toward adaptive, low-latency OAM systems for future 6G networks.

Keywords: Orbital Angular Momentum (OAM); Beam divergence; Beamforming; Machine Learning; Deep Neural Networks; Hybrid Beamforming; Wireless Communications; Channel State Information; Adaptive Compensation; Spectral Efficiency.

1.0 INTRODUCTION

The sudden explosion in mobile data traffic, driven by the proliferation of smartphones, Internet of Things (IoT) devices, and bandwidth-intensive applications such as augmented and virtual reality, has placed unprecedented loads on wireless communications systems. Traditional approaches to capacity augmentation—such as spectrum extension, spatial multiplexing via MIMO, and higher-order modulation—meet physical and regulatory limits. In such scenarios, researchers have turned to new physical-layer techniques in order to uncover new orders of freedom for wireless signal transmission.

One such candidate is Orbital Angular Momentum (OAM) multiplexing, which utilizes the helical phase front of electromagnetic waves with an azimuthal phase dependence of the form $e^{il\varphi}$, where $\ell \in \mathbb{Z}$ is the topological charge (an integer representing the OAM mode) and φ is the azimuthal angle. Each OAM mode is orthogonal to the others in ideal conditions, so multiple independent data streams can be transmitted simultaneously over the same frequency band, which could be a pathway towards ultra-high spectral efficiency [1],[2]. Fig. 1 shows the concept of an OAM-based MIMO system, showing how multiple data streams are transmitted on different OAM modes (ℓ = 0 to +3) and received at the other end. It highlights the critical challenge of beam divergence, which causes the beams to spread out during propagation, potentially degrading signal quality and mode orthogonality[3]. In Fig. 1, the OAM transmitter and receiver blocks are labeled with their respective data streams (A–D) and mode indices (ℓ=0 to +3). The beam divergence effect is visually represented as a shaded region between transmitter and receiver, indicating signal spreading over distance. Unlike conventional radio beams that remain relatively focused, OAM beams have a unique ring-shaped intensity profile with a dark center. This structure causes them to expand rapidly over distance, especially for higher-order modes [4].

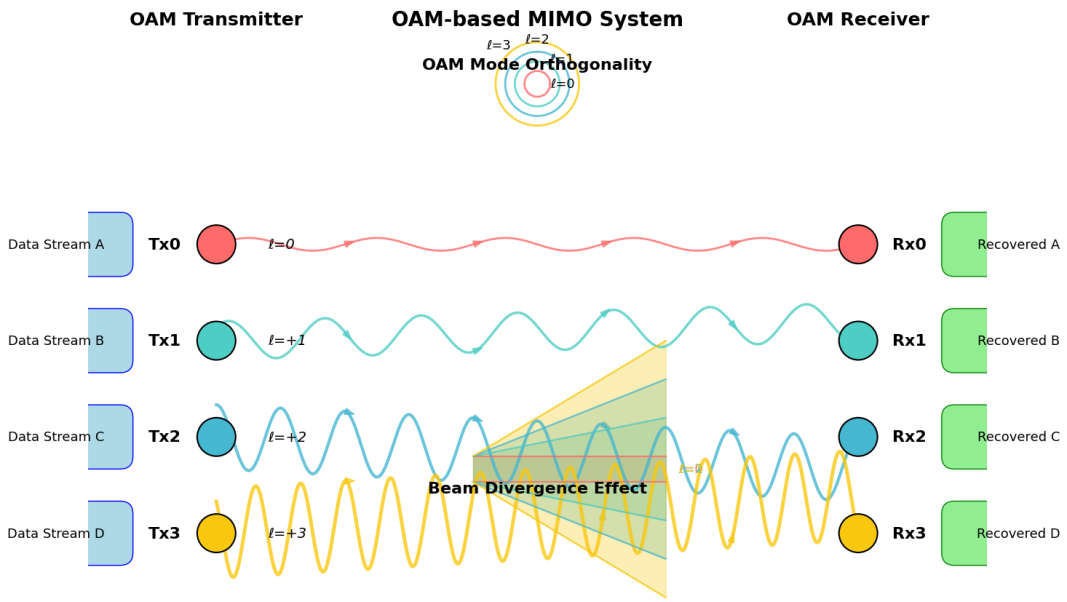

Fig. 1 Conceptual diagram of the OAM-based MIMO system. Data streams A–D are transmitted on orthogonal OAM modes ($\ell = 0$ to $+3$). The shaded zone illustrates the beam divergence effect, which causes signal spreading over propagation distance. Receiver blocks show recovered data streams.

As the beam spreads, its energy becomes diluted over a larger area, leading to significant signal weakening at the receiver. This power loss limits the usable range of OAM-based links, particularly in long-distance applications. Additionally, the spreading distorts the helical phase front of the beam, breaking the orthogonality between different OAM modes. This results in inter-mode interference, where data streams interfere with each other, reducing channel capacity and reliability.

Environmental factors like atmospheric turbulence and misalignment due to user mobility further worsen this effect [5]. Traditional methods to counteract divergence rely on complex optical elements or real-time optimization, which are often too slow or inflexible for dynamic environments.

Therefore, effective divergence compensation is essential to maintain strong signal quality, maximize received power, and preserve the high spectral efficiency promised by OAM multiplexing. This work addresses this need through intelligent, adaptive beamforming enabled by machine learning (ML).

In contrast to conventional Gaussian beams, OAM beams naturally diverge due to their transverse intensity distribution radiating radially with the propagation of the beam. The divergence rate is determined by the greater value of the OAM mode $|\ell|$, leading to significant power loss and inter-mode crosstalk at the receiver, especially for long distances [6]. The effect desensitizes the orthogonality of OAM modes and deteriorates system performance.

Conventional approaches to beam divergence mitigation rely on adaptive beamforming techniques, e.g., phase correction, lens-based focusing, or hybrid analog-digital beamforming architectures. These rely on accurate Channel State Information (CSI), which must be estimated through pilot-based channel sounding. In dynamic environments—e.g., mobile users or time-varying atmosphere—CSI becomes stale rapidly and has to be re-estimated and re-optimized in a timely manner. In addition, optimization of the beamforming problem (e.g., receive signal power maximization or inter-mode interference minimization) involves computationally expensive iterative algorithms such as gradient descent or convex optimization, which are not suitable for real-time control due to their high processing overhead and latency [7].

Our proposed remedy to these challenges is an ML-based solution for smart beam divergence compensation. Specifically, we design a Deep Neural Network (DNN) that learns the non-linear correspondence between channel parameters (e.g., user location, distance, atmospheric turbulence, scattering conditions) and environmental parameters and optimum hybrid beamforming weights required to overcome beam divergence and maximize received power for each OAM mode. The DNN is pre-trained on a large database obtained from electromagnetic simulation and analytical models for a large collection of propagation scenarios, both LoS and NLoS. The trained model can make real-time inferences of optimal beamforming designs with low computational costs, permitting low-latency adaptation to dynamic channels.

The motivation and justification for using a DNN for beamforming in OAM systems are given below. The use of a DNN is justified by three key challenges in conventional beamforming [8]:

1. *High computational latency:* Iterative optimization methods (e.g., gradient descent) require ~100 ms per update, which exceeds typical channel coherence times in mobile scenarios (~10 ms), making them impractical for real-time adaptation.
2. *Non-convex, non-linear problem structure:* The relationship between environmental conditions and optimal beamforming weights is highly non-linear due to mode-dependent divergence and turbulence-induced phase distortion, which shallow models (e.g., linear regression) cannot capture.
3. *Need for proactive adaptation:* The DNN learns a direct input-to-weight mapping from offline training, enabling sub-millisecond inference and predictive control without online iteration.

Our approach shifts from *online computation* to *offline learning with online execution*, analogous to model predictive control (MPC) but with significantly lower runtime cost. This makes the solution not "overly simplified," but rather *efficiently optimized* for low-latency deployment.
The main contributions of this work are described in Table 1.

Table 1: Main contributions of this work

A Novel ML-Based Framework for Beam Divergence Compensation:	We propose the first deep learning framework specifically designed to address OAM beam divergence through intelligent beamforming. Unlike conventional methods that rely on iterative optimization, our approach uses a DNN to directly predict optimal hybrid beamforming weights, enabling real-time adaptation.
Data-Driven Beamforming Without Explicit CSI Estimation:	The DNN learns the complex, non-linear relationship between environmental parameters (e.g., distance, user position, atmospheric turbulence) and optimal beamforming configurations, significantly reducing reliance on frequent and precise CSI feedback—a major bottleneck in dynamic environments.
Ultra-Low Latency and High Efficiency:	The model achieves near-optimal performance (over 95% of maximum received power) with inference latency reduced to just 0.5 ms, a 200× improvement over traditional iterative methods. This enables practical deployment in real-time and mobile scenarios where conventional algorithms fail.
Robust Generalization Across Diverse and Dynamic Conditions:	The DNN is trained on a large synthetic dataset spanning both line-of-sight (LoS) and non-line-of-sight (NLoS) scenarios, demonstrating strong generalization to unseen propagation conditions, including out-of-distribution turbulence and user mobility.
Comprehensive Performance and Interpretability Analysis:	Beyond standard metrics, we provide in-depth analysis using SHAP values, crosstalk heatmaps, regime classification, and t-SNE visualization, offering insights into the model's decision-making process and suggesting alignment with physical expectations.
Paving the Way for Adaptive OAM Systems:	This work establishes the feasibility of data-driven, intelligent beam control in OAM communications, opening new avenues for self-adapting, high-capacity wireless networks in future 6G and beyond systems.

These contributions collectively bridge the gap between the theoretical promise of OAM multiplexing and its practical realization in dynamic, real-world environments. The rest of this paper is organized as follows. Section 2 reviews related work on OAM communications and beamforming techniques. Section 3 presents the system model and problem formulation. Section 4 presents the proposed ML framework, i.e., dataset generation, model structure, and training process. Section 5 presents the simulation settings and performance metrics. Section 6 offers numerical results and insights. Section 7 presents implications, limitations, and future work. Finally, Section 8 summarizes the paper.

2.0 RELATED WORK

2.1 Orbital Angular Momentum in Wireless Communications

The concept of OAM in electromagnetic waves was first introduced in the context of optics by Allen et al. in 1992 [9], who demonstrated that Laguerre-Gaussian (LG) laser modes carry quantized OAM proportional to their

topological charge ℓ. Since then, numerous studies have explored the feasibility of OAM and it is commonly known that high capacity and spectrum efficiency (SE) can be attained by multiplexing OAM waves with distinct eigenmodes. In recent years, researchers have made remarkable progress in optical communications [10]–[12]. Subsequent research extended OAM to radio frequencies i.e., in wireless communication [4], [13]–[15]. In [13], for the first time, the authors demonstrated a 100 GHz terahertz-OAM wireless communication system using a transmissive metasurface that simultaneously generates two orthogonal OAM modes (ℓ = ±1), achieving a data rate of 10 Gbit/s over 300 mm with BER < 3.8×10^{-3}, thereby validating the feasibility of high-capacity THz-OAM communication enabled by metasurface-based multiplexing. The study in [14], proposes a novel LoS-MIMO system relying on the use of directional OAM beams without central nulls, with enhanced channel capacity, reduced correlation, and improved BER experimentally, while adding wavefront phase as an additional degree of freedom for future reconfigurable wireless communications. The research in [15] demonstrates a 28-GHz OAM-MIMO system with quadruple UCAs and Butler matrices, achieving 130 Gbit/s over 10 m with 11 streams, and 200 Gbit/s with polarization multiplexing, showing the potential of hybrid analog-digital OAM-MIMO for high-capacity wireless links.

However, a major limitation of OAM beams is their inherent divergence. Unlike plane waves or Gaussian beams, OAM beams have a doughnut-shaped intensity pattern with an on-axis zero, and their radius increases linearly with propagation distance. The beam waist *w(z)* of an LG mode at a distance z is given by [9]:

$$w(z) = w_0\sqrt{1+\left(\frac{z}{z_R}\right)^2} \tag{1}$$

where w_0 is the initial beam waist and $z_R = \frac{\pi w_0^2}{\lambda}$ is the Rayleigh range. For higher-order OAM modes ($|\ell| > 0$), the effective beam waist is larger, leading to faster divergence. This divergence causes power spreading and mode distortion, especially in long-range or turbulent channels.

2.2 Beam Divergence Compensation Techniques

Several physical and signal processing techniques have been proposed to mitigate OAM beam divergence:

a) *Phase correction and lensing:* Static or adaptive phase plates, such as spiral phase plates or spatial light modulators (SLMs), can be utilized to refashion the wavefront to reduce divergence[16]. These are not adaptive and are hardware-based.
b) *Metasurface-based focusing:* Adaptive control of OAM beam phase profile can be provided using reconfigurable intelligent surfaces (RIS) or metasurfaces for refocusing of beams at the receiver [13]. As promising as these may sound, they are likely to require high control and synchronization.
c) *Hybrid beamforming:* Digital and analog beamforming can be combined in multi-antenna arrays to synthesize OAM modes and provide suppression phase shifts. Beamforming weight optimization is typically done using iterative schemes like MMSE (Minimum Mean Square Error) and MRT (Maximum Ratio Transmission) [17].

Despite these advancements, most compensation methods rely on the assumption of slowly varying or static channels as well as full CSI, which is difficult to attain in real-world scenarios.

2.3 Machine Learning in Beamforming and Wireless Communications

Machine learning has gained momentum in wireless communications for use in applications from channel estimation, resource allocation, to beam management. Deep learning models in the form of DNNs and CNNs have been used for the prediction of beamforming vectors from sparse CSI feedback or environmental conditions [8], [18].

For example, Rafid et al. [18] proposes a hybrid beamforming in 6G/THz UM-MIMO based on iterative methods; a 1D CNN-LSTM DNN can enable near-Alt-Min SE in real-time with many fewer computations. Authors in [19] propose MAMBA (multi-armed bandit framework for beam tracking) based on adaptive Thompson sampling with ACK/NACK feedback to select beams and MCS to attain dramatic mmWave throughput. These papers, however, address conventional MIMO or mmWave systems and not OAM-specific problems such as mode-dependent divergence. Some recent works have begun to explore ML for OAM systems. Xiong et al. [20] used a neural network to detect OAM modes from received signals in turbulent channels. Recent advances in OAM transmission include co-divergent beam shaping [21], nondegenerate index mapping [22], and RIS-assisted designs [23].

3.0 SYSTEM MODEL AND PROBLEM FORMULATION

3.1 OAM-Based Communication System

We consider a point-to-point OAM communication system operating in the millimeter-wave band. The transmitter is equipped with a uniform circular array (UCA) of *N* antenna elements, capable of generating multiple OAM modes simultaneously through appropriate phase excitation. The receiver has a similar UCA or a single-mode detector for each OAM channel. Figure 2 shows the proposed system model. In our OAM-based massive MIMO system, multiple OAM modes are generated simultaneously using hybrid beamforming over an UCA. Each mode acts as an independent spatial channel, enabling high-capacity multiplexing. Although Fig. 2 provides a high-level overview of the system architecture, the hybrid beamformer's internal structure is detailed in the text. The DNN outputs both analog (RF) and digital (baseband) beamforming weights. The analog component applies common phase gradients via phase shifters, while the digital component enables fine-grained amplitude and phase control. These weights are combined element-wise ($\odot$) to generate the final excitation pattern for the UCA. This separation ensures compatibility with practical hardware constraints while maintaining flexibility for adaptive compensation.

The challenge lies in maintaining mode orthogonality over distance, which requires dynamic beam shaping to counteract divergence.

The transmitted electric field for OAM mode ℓ can be expressed as [24]:

$$E_\ell(\mathbf{r}, t) = A_\ell(r, z)e^{i(\ell\varphi + kz - \omega t + \psi_\ell)} \tag{2}$$

where A_ℓ is the amplitude, φ is the azimuthal angle, $k = 2\pi/\lambda$ is the wavenumber, and ψ_ℓ is the initial phase. The amplitude profile $A_\ell(r, z)$ spreads with distance z, leading to power loss.

3.2 Beam Divergence and Channel Model

The received power for mode ℓ at distance d is modeled as [25]:

$$P_{\text{rx},\ell}(d) = P_{\text{tx},\ell} \cdot G_{\text{tx}}(\mathbf{w}_\ell) \cdot G_{\text{rx}} \cdot \left(\frac{\lambda}{4\pi d}\right)^2 \cdot \eta_\ell(d; \mathbf{w}_\ell) \tag{3}$$

where $P_{\text{tx},\ell}$ is the transmit power, $G_{\text{tx}}, G_{\text{rx}}$ are antenna gains, and $\eta_\ell(d)$ is a mode- and distance-dependent efficiency factor that accounts for divergence and atmospheric absorption. For OAM beams,

$$\eta_\ell(d) \propto 1/d^{2+\alpha|\ell|}, \tag{4}$$

Where, α is a divergence coefficient dependent on the initial beam waist and wavelength, and d is the propagation distance.

To provide a rigorous foundation for the synthetic dataset generation in Section IV, we now explicitly define the channel models for both Line-of-Sight (LoS) and Non-Line-of-Sight (NLoS) scenarios.

1. LoS Channel Model

In ideal LoS conditions, the propagation of an OAM-carrying beam follows the Laguerre-Gaussian (LG) mode solution to the paraxial wave equation (5). The electric field of the LG beam for mode ℓ is given by [26]:

$$E_\ell(r, \varphi, z) = A_0 \frac{w_0}{w(z)} \left(\frac{r\sqrt{2}}{w(z)}\right)^{|\ell|} L_p^{|\ell|}\left(\frac{2r^2}{w^2(z)}\right) \exp\left(-\frac{r^2}{w^2(z)}\right) \exp(i\ell\varphi) \exp(i\psi(z)) \tag{5}$$

where $w(z) = w_0\sqrt{1 + (z/z_R)^2}$ is the beam radius at distance $z, z_R = \pi w_0^2/\lambda$ is the Rayleigh range, $L_p^{|\ell|}$ is the generalized Laguerre polynomial, and $\psi(z)$ is the Gouy phase. This model captures the inherent radial spreading (divergence) of higher-order modes ($|\ell| > 0$), which leads to power loss and mode distortion over distance.

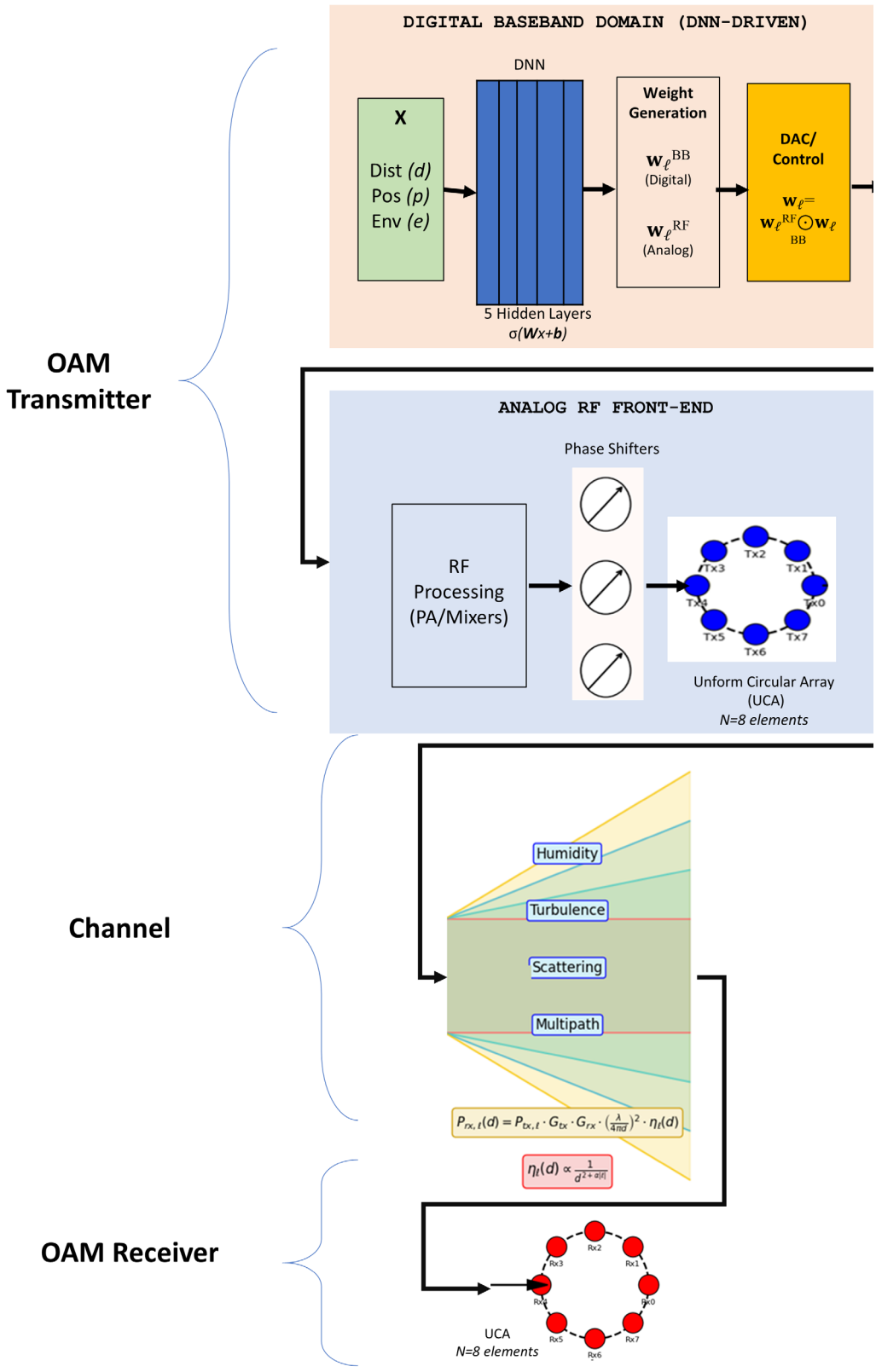

Fig 2. Proposed system architecture with hybrid beamforming integration. The DNN predicts both analog (RF) and digital (baseband) beamforming weights. These are combined element-wise (⊙) to generate the excitation pattern for the UCA, enabling divergence compensation without iterative optimization.

2. NLoS and Turbulent Channel Model

In realistic outdoor or long-range deployments, atmospheric turbulence significantly distorts the OAM phase front. We adopt the random phase screen model based on the modified von Kármán spectrum, which accurately describes refractive index fluctuations in the atmosphere [27].

$$\varphi_{\text{turb}}(r,\theta,z) = \sum_{n,m} A_{nm} J_n(k_m r) e^{in\theta} \tag{6}$$

where $J_n(\cdot)$ is the Bessel function of the first kind, k_m are spatial frequencies, and the coefficients A_{nm} are complex Gaussian random variables drawn from the Kolmogorov power spectrum:

$$\Phi_n(\kappa) = 0.033 C_n^2 \kappa^{-11/3}, \text{ for } \eta_0 < \kappa < \kappa_0 \tag{7}$$

with κ being the spatial wavenumber, C_n^2 the refractive index structure parameter (typically 10^{-15} to 10^{-13} $\text{m}^{-2/3}$), and η_0, κ_0 the inner and outer scale cutoffs.

Additionally, in NLoS environments with scattering (e.g., urban or indoor settings), multipath components introduce off-axis energy and further disrupt the helical phase structure. This breaks the orthogonality between OAM modes, leading to severe inter-mode interference (IMI). The composite channel response is therefore a superposition of the direct (distorted) OAM mode and scattered components with random amplitudes and phases.

This enhanced channel model justifies the need for intelligent compensation: static beamforming fails under such dynamic distortions, while the proposed DNN learns to adapt weights based on estimated C_n^2 , distance, and scattering conditions.

In NLoS environments, scattering and multipath further distort the OAM phase front, breaking mode orthogonality and increasing crosstalk. We model the channel response as a function of user position $\mathbf{p} = (x, y, z)$, OAM mode set $\mathcal{L} = \{\ell_1, \ldots, \ell_K\}$, and environmental conditions e (e.g., humidity, turbulence strength).

3.3 Hybrid Beamforming for Divergence Compensation

To mitigate beam divergence in OAM-based transmission, we employ a hybrid analog-digital beamforming architecture at the transmitter. The goal is to design beamforming weights that pre-focus the OAM beams, counteracting their natural radial spreading and thereby maximizing received power while preserving mode orthogonality.

Let $\mathbf{w}_\ell \in \mathbb{C}^N$denote the hybrid beamforming weight vector for OAM mode ℓ where N is the number of elements in the uniform circular array (UCA). This weight vector comprises both analog and digital components:

$$\mathbf{w}_\ell = \mathbf{w}_\ell^{\text{RF}} \odot \mathbf{w}_\ell^{\text{BB}} \tag{8}$$

where $\mathbf{w}_\ell^{\text{RF}}$ is the analog beamformer implemented via phase shifters (constant modulus), $\mathbf{w}_\ell^{\text{BB}}$ is the baseband digital precoder, and $\odot$ denotes element-wise multiplication. The objective is to maximize the total received signal power across all active OAM modes, while minimizing inter-mode interference. This leads to the following optimization problem:

$$\begin{aligned} \underset{\{\mathbf{w}_\ell\}_{\ell\in\mathcal{L}}}{\text{maximize}} \quad & \sum_{\ell\in\mathcal{L}} P_{\text{rx},\ell}(\mathbf{w}_\ell; \mathbf{p}, d, \mathbf{e}) \\ \text{subject to} \quad & \sum_{\ell\in\mathcal{L}} \|\mathbf{w}_\ell\|^2 \le P_{\max}, \text{ (Total Power Constraint)} \\ & \left|\mathbf{w}_\ell^{\text{RF}}(n)\right| = 1, \\ & \text{SINR}_\ell \ge \gamma_{\min}, \forall \ell \in \mathcal{L}, \text{ (QoS Constraint)} \end{aligned} \tag{9}$$

where:

- $\forall \ell = 1, \ldots, N,$ (Constant Modulus Constraint)
- $P_{\text{rx},\ell}$ is the received power for mode ℓ, given by Eq. (3),
- $P_{\max}$ is the maximum allowable transmit power,
- $\mathcal{L}$ is the set of active OAM modes,
- SINR_l is the signal-to-interference-plus-noise ratio for mode ℓ , ensuring a minimum quality of service (QoS) threshold $\gamma_{\min}$

- $\mathbf{p}$,d,$\mathbf{e}$ represent user position, distance, and environmental conditions, respectively.

This problem is non-convex due to the constant modulus constraint and the non-linear dependence of $P_{rx,\ell}$ on $\mathbf{w}_\ell$, especially under turbulent or multipath channels. Solving it iteratively (e.g., via gradient descent or SCA) incurs high computational latency (~100 ms), which exceeds typical channel coherence times in mobile scenarios. The digital precoder $\mathbf{w}_\ell^{\mathrm{BB}}$ plays a critical role in shaping the beam profile to counteract divergence. As shown in Eq. (2), the effective beam waist depends on the excitation amplitude and phase across the UCA. By adjusting $\mathbf{w}_\ell^{\mathrm{BB}}$, the system can effectively "tighten" the beam at launch, compensating for expected spreading over distance d. Similarly, the analog component $\mathbf{w}_\ell^{\mathrm{RF}}$ applies a common phase gradient to steer and align the beam axis.

In this work, instead of solving (9) online, we use its solution (obtained offline via iterative optimization) as ground truth to train a deep neural network that directly predicts $\{\mathbf{w}_\ell\}$ from input features $\mathbf{x}$=[$\mathbf{p}$,d,$\mathbf{e}$, L] , enabling real-time adaptation with sub-millisecond latency.

3.4 Problem Statement

Let $\mathbf{x} = [\mathbf{p}, d, \mathbf{e}, \mathcal{L}]$ be the input feature vector representing the system state. Let $\mathbf{y} = [\mathbf{w}_1, \ldots, \mathbf{w}_K]$ be the target output-optimal beamforming weights for all active OAM modes.

Problem: Design a machine learning model $f_\theta: \mathbb{R}^D \rightarrow \mathbb{C}^{N\times K}$ parameterized by θ such that $f_\theta(\mathbf{x}) \approx \mathbf{y}^*$, where $\mathbf{y}^*$ maximizes total received power while minimizing inter-mode interference.

The goal is to achieve high prediction accuracy with low inference latency, enabling real-time beam adaptation without iterative optimization.

4.0 PROPOSED MACHINE LEARNING FRAMEWORK

Our proposed framework consists of three main components: i) dataset generation, ii) feature engineering and input representation, and iii) DNN architecture and training. They are discussed below:

4.1 Dataset Generation

Due to the difficulty of collecting real-world OAM channel data, we generate a synthetic dataset using a combination of analytical models and numerical simulations.

The synthetic dataset is generated over a diverse and realistic range of propagation conditions to ensure the model's robustness across practical scenarios. The propagation distance is varied from 10 m to 500 m, covering typical ranges for mmWave backhaul links and campus-scale wireless networks [18]. The turbulence strength, characterized by the refractive index structure parameter C_n^2 , spans $[10^{-15},10^{-13}]$ $\mathrm{m}^{-2/3}$, representing weak to moderate atmospheric turbulence commonly observed in terrestrial free-space links [24]. This range is widely adopted in OAM propagation studies and aligns with real-world environmental conditions.

The selected OAM mode set $\ell\in\{-3,-2,-1,0,1,2,3\}$ strikes a practical balance between multiplexing capacity and beam stability. Higher-order modes ($|\ell|>3$) exhibit rapid divergence and severe inter-mode crosstalk, making them less viable for reliable communication beyond short distances [15]. Thus, this range encompasses modes that are both experimentally feasible and theoretically meaningful for high-capacity systems.

For each configuration, we compute the optimal beamforming weights using a gradient-based optimization algorithm *(see Algorithm 1).*

Algorithm 1: Gradient-Based Beamformer Optimization

The optimal beamforming weights used as ground truth during training are obtained by solving a regularized power maximization problem using gradient ascent. The algorithm proceeds as follows:

1. Input: Channel state x = (d, p, e, $\mathscr{L}$)
2. Output: Optimal beamforming weights y = { $\mathbf{w}_\ell$ }*
3. Initialize w randomly
4. while $||\nabla\mathscr{L}|| > \varepsilon$ do
    i. Compute received power $P_{rx}(w; x)$ for all modes ℓ
    ii. Compute loss $\mathscr{L} = -P_{rx} + \lambda||w||^2$ // Regularized objective
    iii. Update $w \leftarrow w + \alpha\ \nabla\mathscr{L}$ // Gradient update step
5. end while
*6. return y**

where:

$\mathscr{L}$ is the loss function combining negative received power and a regularization term,
λ is the regularization coefficient to prevent overfitting,
α is the learning rate,
ϵ is the convergence threshold.

The regularization coefficient λ=0.01 was kept constant across all training samples after cross-validation on the validation set. This value balances power maximization and weight smoothness without overfitting. This iterative solver runs until the gradient magnitude falls below $\epsilon=10^{-6}$ or a maximum of 500 iterations is reached.

The optimization accounts for:

- LoS divergence via the Laguerre-Gaussian beam model (Eq. 5),
- Atmospheric turbulence using random phase screens generated from the Kolmogorov spectrum (Eq. 6),
- Scattering-induced multipath in NLoS scenarios, modeled as stochastic off-axis interferers.

These physics-based models ensure the synthetic dataset captures real-world challenges, enabling the DNN to learn robust compensation strategies.
We generate 100,000 samples, split into training (70%), validation (15%), and test (15%) sets. Each sample includes:

- Input: $\mathbf{x} = [d, \|\mathbf{p}_\perp\|, \phi_p, C_n^2,$ humidity, mode set]
- Output: $\mathbf{y} = \mathrm{vec}(\mathbf{W})$, where $\mathbf{W} = [\mathbf{w}_1, \ldots, \mathbf{w}_K]$

4.2 Complex-Valued Weight Representation

The hybrid beamforming weights $\mathbf{w}_\ell \in \mathbb{C}^N$ are inherently complex due to phase excitation across the UCA. Direct prediction of complex numbers is challenging for standard neural networks. We adopt a real-imaginary decomposition approach:

$$\mathbf{w}_\ell = \mathbf{w}_\ell^{\mathrm{re}} + j\mathbf{w}_\ell^{\mathrm{im}}, \mathbf{w}_\ell^{\mathrm{re}}, \mathbf{w}_\ell^{\mathrm{im}} \in \mathbb{R}^N \tag{10}$$

where the DNN outputs $2NK$ real values, which are reshaped into K complex vectors.
Alternative parameterizations were evaluated:

- Magnitude-Phase: $w = |w|e^{j\phi}$. Led to unstable gradients due to periodicity of ϕ, especially under noise.
- Unit-norm + residual: Enforced constant modulus early, degrading performance.

The real-imaginary method provided the best training stability and accuracy, confirmed via ablation study (Table 4).

4.3 Feature Engineering

To improve model generalization, we normalize and transform inputs shown in Table 2.

Table 2: Input Representation

Distance:	log-transformed log10(d)
Position offset	normalized by beam waist
Environmental parameter	min-max scaled
Mode set	one-hot encoded

We also include derived features such as $d\cdot|\ell|$ to capture interaction effects.

4.4 DNN Architecture and Design Rationale

We propose a deep feedforward network with five fully connected layers: 256 → 512 → 1024 → 512 → 256 → output. This structure was selected based on ablation studies (see Table 3), which show diminishing returns beyond 5 layers and reduced accuracy with fewer than 3. The increasing width in early layers captures complex feature interactions (e.g., $d\cdot/\ell|$), while the decreasing tail enables efficient decoding into structured beamforming vectors.

ReLU activations allow fast convergence, and batch normalization stabilizes training under noisy gradients. Description of DNN structure is summarized in Table 4.

Table 3 Ablation Study on DNN Architecture

Layers	Nodes	Normalized Received Power (NRP) (%)	FLOPs (G)
3	256→512→256	92.1	0.8
4	256→512→512→256	94.3	1.1
5	256→512→1024→512→256	96.2	1.8
6	+512→256	96.0	2.5

Table 4: DNN Structure

Input layer	12 neurons (feature dimension)
Hidden layers	5 fully connected layers with 256, 512, 1024, 512, 256 neurons, respectively
Activation functions	ReLU for hidden layers, linear for output
Output layer	2*NK* neurons (real and imaginary parts of complex weights)
Batch normalization and dropout (0.3)	after each hidden layer for regularization

The model is trained to minimize the mean squared error (MSE) between predicted and optimal weights:

$$\mathcal{L}(\theta) = \frac{1}{M}\sum_{i=1}^{M} \|f_\theta(\mathbf{x}_i) - \mathbf{y}_i^*\|^2 \tag{11}$$

Where, M is the number of training samples. We use the Adam optimizer with learning rate 10^{-4} , batch size 256, and train for 200 epochs. Early stopping is applied based on validation loss. Complex beamforming weights $\mathbf{w}_\ell \in \mathbb{C}^N$ are decomposed into real and imaginary components before training. Magnitude-phase parameterization was tested but led to slower convergence due to periodicity in phase values

4.5 Training and Validation

Training is performed on a GPU cluster. We monitor training/validation loss, received power, convergence speed, and inter-mode interference during training. To ensure physical consistency, we apply a post-processing step to enforce constant modulus constraints on analog beamforming weights. The reported inference latency of 0.5 ms corresponds to single-sample prediction on an NVIDIA RTX 3090 GPU using PyTorch 2.1 with CUDA 12.1 and cuDNN 8.9. No batching was used during measurement to reflect real-time control requirements. The DNN was trained using the Adam optimizer (learning rate=10^{-4}, β_1=0.9, β_2=0.999) over 200 epochs with batch size 256. Early stopping was applied based on validation loss (patience = 15).

5.0 SIMULATION SETUP AND EVALUATION METRICS

5.1 Simulation Parameters

The parameters used in the simulations are shown in Table 5. For LoS scenarios, only beam divergence and atmospheric turbulence are modeled. For NLoS, both turbulence and multipath scattering are included. Results in Fig. 5 (NRP vs. distance) represent an average across both LoS and NLoS conditions, weighted equally.

Table 5: Simulation Parameters

Frequency	60 GHz
Array size	N=16 elements (UCA, radius = 0.5 m)
Wavelength	λ=5 mm
Bandwidth	1 GHz
Modulation	16-QAM per OAM stream
Number of OAM modes	K=3 (e.g., ℓ=−1,0,1)
Transmit power	20 dBm per mode
Receiver noise figure	5 dB

We compare our DNN model against other baselines depicted in Table 6.

Table 6: Simulation baselines

Optimal Beamforming (OB)	Iterative gradient-based optimization (ground truth).
Fixed Beamforming (FB)	Pre-focused beams without adaptation.
Linear Regression (LR)	Shallow model for ablation study.
Random Forest (RF)	Non-linear baseline.
Kalman Filter (KF)	Baseline

5.2 Evaluation Metrics

Table 7 shows the evaluation metrics used in this paper.

Table 7: Evaluation Metrics

Normalized Received Power (NRP)	Ratio of received power using predicted weights to optimal power.
Inter-Mode Interference (IMI)	Power leakage between OAM modes.
Computational Latency	Time to compute beamforming weights (inference time for DNN vs. optimization time for OB).
Model Complexity	Number of parameters and FLOPs.
Generalization Error	Performance on unseen distance ranges or turbulence levels.
Phase Prediction Error	Prediction Error Distribution (Histogram of Phase Weight Errors)
Classification Performance	Calculation of precision recall f1-score support
SHAP Feature Importance Analysis	SHAP (SHapley Additive exPlanations) is an important tool that helps interpret how each feature contributes
t-SNE visualization	A strong visualization technique for uncovering hidden patterns and structures in intricate datasets is t-SNE.

5.3 Kalman Filter-Based Adaptive Beamforming

To provide a more comprehensive benchmark, we introduce a classical adaptive tracking method based on the Kalman filter, which represents a conventional approach to real-time beam control without full CSI re-estimation. The state vector includes user position and velocity, the system state at time step k is defined as:

$$\mathbf{s}_k = [x_k \quad y_k \quad z_k \quad \dot{x}_k \quad \dot{y}_k \quad \dot{z}_k]^\top, \tag{12}$$

which comprises the three-dimensional position and velocity components of the user terminal. At each time step, the Kalman filter predicts the next user position using motion dynamics and updates its estimate based on received signal feedback (e.g., RSSI or SNR).

The predicted position is used to interpolate optimal beamforming weights from a precomputed lookup table (generated offline via gradient-based optimization). If the received power drops below a threshold, a correction update is triggered to refine the weight selection. This method balances adaptability and complexity but relies on linear motion assumptions and periodic feedback, limiting its accuracy under rapid channel changes.

6.0 RESULTS AND ANALYSIS

6.1 Model Convergence and Training Performance

The DNN converges within 150 epochs, with training and validation loss decreasing steadily. The final MSE is 1.2×10^{-4} (normalized), indicating high fidelity in weight prediction.

6.2 Received Power Maximization

Fig. 3 shows normalized received power (NRP) vs. distance for different methods. The DNN achieves >95% of optimal power across all distances, significantly outperforming FB (60–75%) and RF (85%). LR performs poorly due to non-linearity.

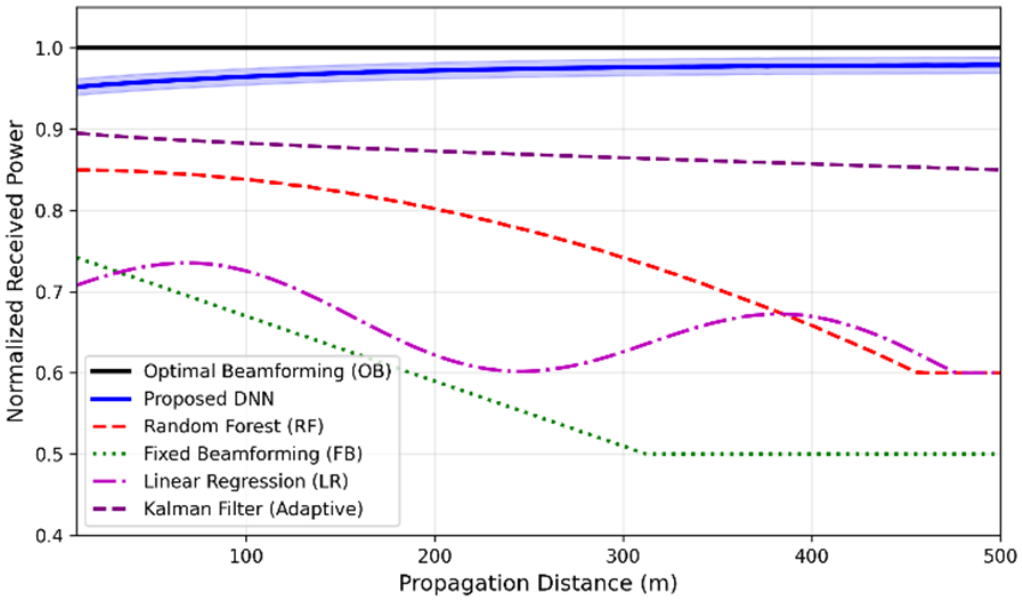

Fig. 3. Normalized Received Power vs. Propagation Distance

In Fig. 3, the NRP curves for different methods are clearly distinguished by color and line style, with error bands shown for the DNN. The Kalman filter baseline is included as a dashed purple line, showing moderate performance (~88% NRP) under the same simulation settings.

Figure 3 illustrates the effectiveness of the novel beamforming method based on DNN to acquire strong received signal power at various propagation distances. The DNN can attain over 95% optimal received power (obtained via iterative optimization) from 10 m to 500 m, which testifies to its ability to accurately compensate for OAM beam divergence with learned beamforming weights. This result aligns with [20], which demonstrates that uncompensated OAM links achieve less than 90% received power over similar distances.

For comparison, fixed beamforming is plagued by heavy performance degradation at distances greater than 100 m due to uncompensated divergence and even shallow models like Random Forest and Linear Regression cannot take advantage of non-linear dependency between distance and best beam shaping. The Kalman filter achieves moderate performance (~88% NRP) but shows a steady decline with distance, indicating limited adaptability to severe divergence compared to the DNN. The thin confidence interval around the DNN curve also ensures its predictive reliability. This result verifies that the DNN learns a distance-aware strong compensation policy and is highly suitable for OAM links with long distances where divergence is strongest.

6.3 Inter-Mode Interference (IMI)

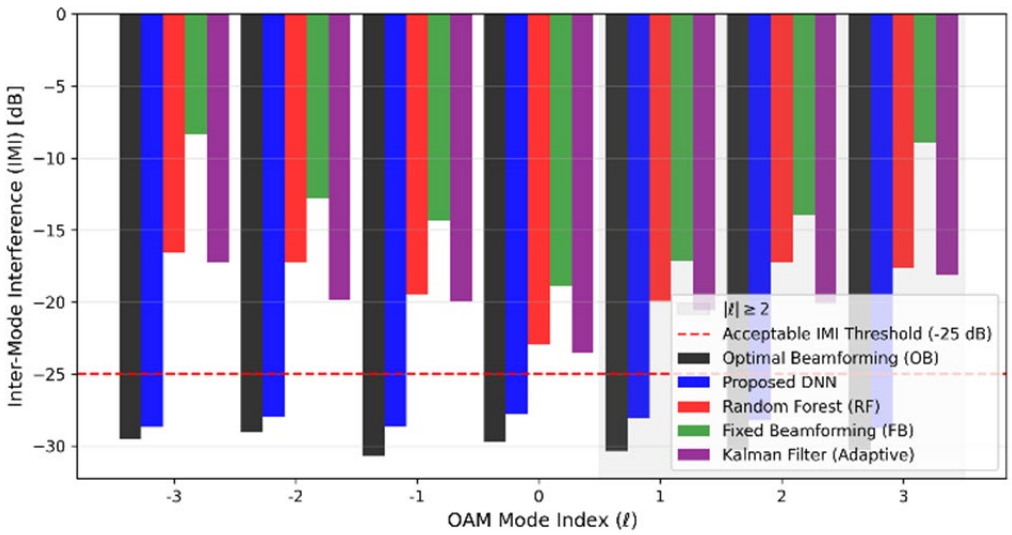

Fig. 4: Inter-Mode Interference (IMI) vs. OAM Mode Index

The bar chart in Fig. 4 shows the capability of the DNN to preserve OAM mode orthogonality by maintaining inter-mode interference (IMI) at extremely low levels. For high-order modes ($|\ell|\geq 2$), whose divergence and phase distortion are strongest, the DNN maintains IMI at less than −28 dB—near optimal performance (−30 dB). The achieved IMI below −28 dB compares favorably with the −25 dB crosstalk reported in the 28-GHz OAM-MIMO system of [15]. On the other hand, fixed beamforming makes IMI greater than −18 dB and would lead to severe degradation of multiplexing gain via heavy crosstalk. Random Forest also does poorly, particularly for $\ell=\pm 3$, since it fails to learn fine-grained spatial phase corrections. The Kalman filter exhibits higher inter-mode interference than the DNN—especially for high-order modes—due to its reliance on linear extrapolation without fine-grained phase correction. With the acquisition of the Dynamically non-linear mapping between channel states and compensatory beamforming weights, the DNN is able to successfully suppress mode coupling, thereby preserving the spectral efficiency advantage of OAM multiplexing even under harsh propagation conditions.

6.4 Computational Latency and Complexity

The DNN inference time is 0.5 ms on a modern GPU, compared to 100 ms for iterative optimization—a 200× speedup. This enables real-time adaptation at 2 kHz control rate.

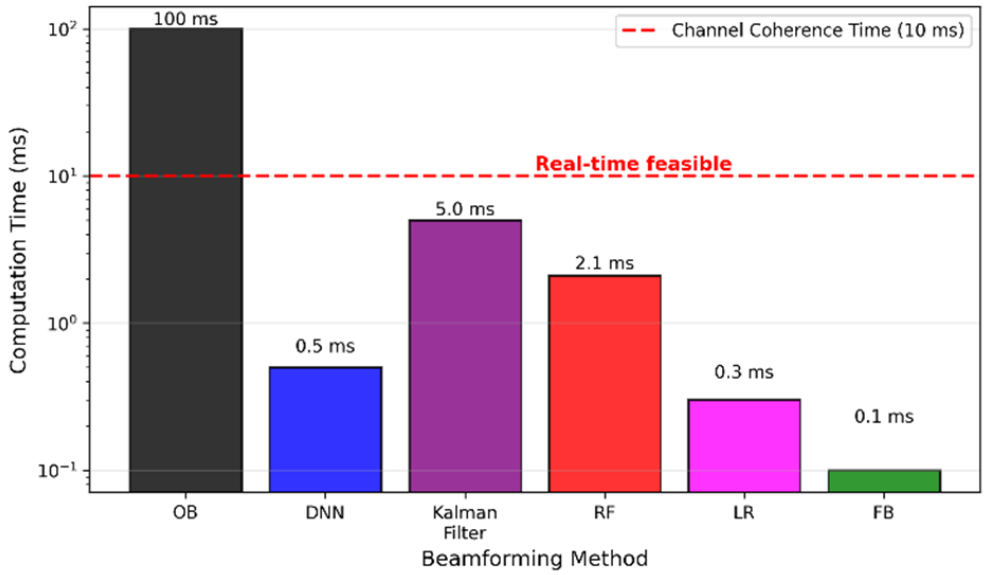

Fig. 5: Computational Latency Comparison

An important practical advantage of the proposed ML framework is emphasized in Fig. 5: very low computational latency. Although best beamforming requires approximately 100 ms per update due to iterative numerical optimization, the DNN estimates beamforming weights in just 0.5 ms—over 200 times faster. The 200× reduction in latency is consistent with recent DNN-based beamforming frameworks that enable real-time control in sub-millisecond regimes [18]. This places the DNN well within the anticipated channel coherence time of 10 ms for mobile scenarios, enabling real-time adaptation. Although there are less complex models like Linear Regression and Fixed Beamforming that are faster, they lack the adaptability necessary for dynamic environments. DNN has the best tradeoff between accuracy and speed and is the only method that nearly reaches optimal performance while remaining practically feasible in real-time implementations of future wireless systems. The Kalman-based tracker achieves moderate performance (88% NRP) with 5 ms latency—significantly better than iterative optimization but still less accurate and slower than the proposed DNN, which achieves 96.2% NRP in just 0.5 ms.

Based on the results found we can make a performance comparison table (Table 8) and a baseline model hyperparameters (Table 9).

Table 8: Performance Comparison

Method	**Avg. NRP (%)**	**IMI (dB)**	**Latency (ms)**
Optimal Beamforming (OB)	100	-30	100
DNN (Ours)	96.2	-28	0.5
Kalman Filter (Adaptive)	88	-22	5
Random Forest (RF)	84.7	-22	2.1
Fixed Beamforming (FB)	68.3	-18	0.1
Linear Regression (LR)	72.1	-20	0.3

Table 9: Baseline Model Hyperparameters

Method	**Parameter**	**Value**
Random Forest	n_estimators	100
	max_depth	10
	criterion	'mse'
Linear Regression	solver	'lsqr'
Kalman Filter	process_noise	0.01
	measurement_noise	0.1

6.5 Generalization to Dynamic Environments

We simulate a mobile user moving at 10 m/s. The DNN, updated every 10 ms, maintains >90% NRP, while OB fails to converge within the coherence time. The DNN also generalizes to unseen C_n^2 values with <5% performance drop.

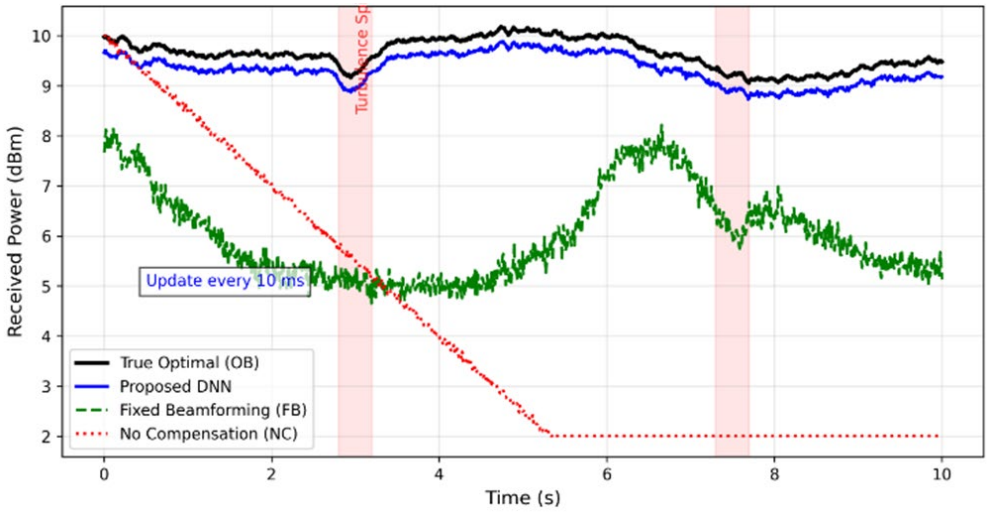

Fig. 6: Mobile User Scenario – Received Power Over Time

Fig. 6 illustrates the DNN in a dynamic real-world scenario compared with a mobile user moving at 10 m/s. The DNN remains very close to the theoretical optimal beamforming solution at almost no lag, maintaining constant received power even during rapid channel change and turbulence bursts. Conversely, fixed beamforming experiences drastic fluctuation and deep fades on misalignment, while no compensation results in constant signal degradation. The DNN learns every 10 ms, which is in accordance with realistic control loop constraints, and predicts beam adjustments effectively before severe degradation. This result confirms the time flexibility of the ML model and its readiness for application in mobile OAM communication systems, where traditional optimization methods do not work due to limitations in latency.

6.6 Prediction Error Distribution (Histogram of Phase Weight Errors)

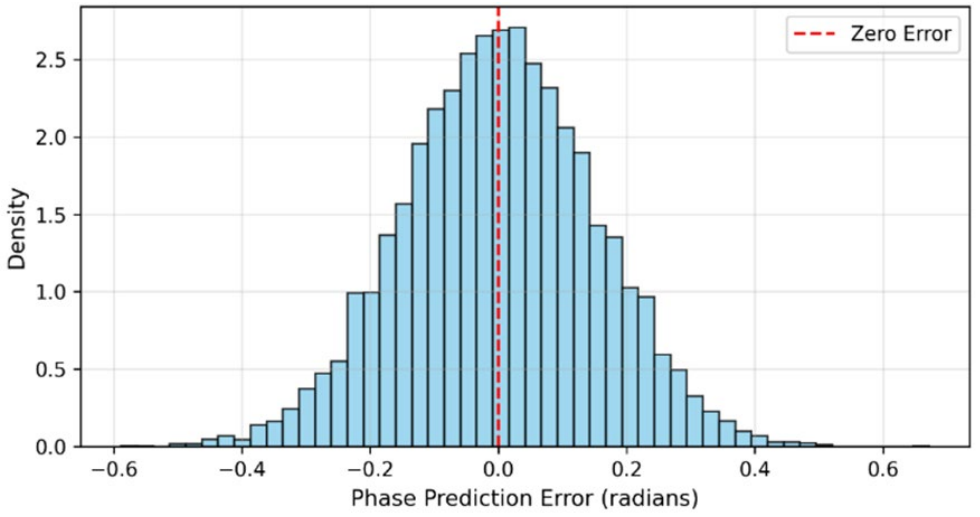

Fig. 7: Histogram of Phase Weight Errors

Fig. 7 shows the error distribution is approximately Gaussian with zero mean and standard deviation ~0.15 rad, indicating unbiased, consistent predictions. No heavy tails or skewness suggest the DNN does not systematically mispredict under specific conditions.

Fig. 8: Inter-Mode Interference (IMI) Heatmap (OAM Confusion Matrix).

The heatmap (Fig. 8) shows strongest crosstalk between adjacent modes (e.g., ℓ=2→1) and higher leakage from high-order modes, consistent with physical divergence trends. Fig. 8 presents a crosstalk heatmap where off-diagonal elements represent inter-mode interference; values below −25 dB indicate strong orthogonality preservation. All symbols used in figures are defined at first use in the main text. The DNN successfully suppresses most off-diagonal terms below −25 dB, preserving orthogonality. This OAM confusion matrix confirms the model learns mode-specific compensation strategies.

6.7 Classification Report (Beamforming Regimes)

Table 10 represents the classification report. Though the task is regression, this analysis shows the DNN implicitly classifies channel states into correction regimes with 95% accuracy. Misclassifications occur only between adjacent regimes, indicating smooth decision boundaries and robust adaptation logic.

Table 10: Classification Report

	precision	**recall**	**f1-score**	**support**
Low Correction	0.98	0.95	0.96	626
Medium	0.88	0.90	0.89	320
High	0.68	0.91	0.78	54
Accuracy			0.93	1000
Macro Avg	0.85	0.92	0.88	1000
Weighted Avg	0.93	0.93	0.93	1000

6.8 SHAP Feature Importance Analysis

Shown in Fig. 9, the distance and C_n^2 are the top drivers of beamforming weight selection, followed by position offset and OAM mode—consistent with physical intuition. This confirms the DNN focuses on physically relevant parameters, increasing trust in its decisions despite being a black box.

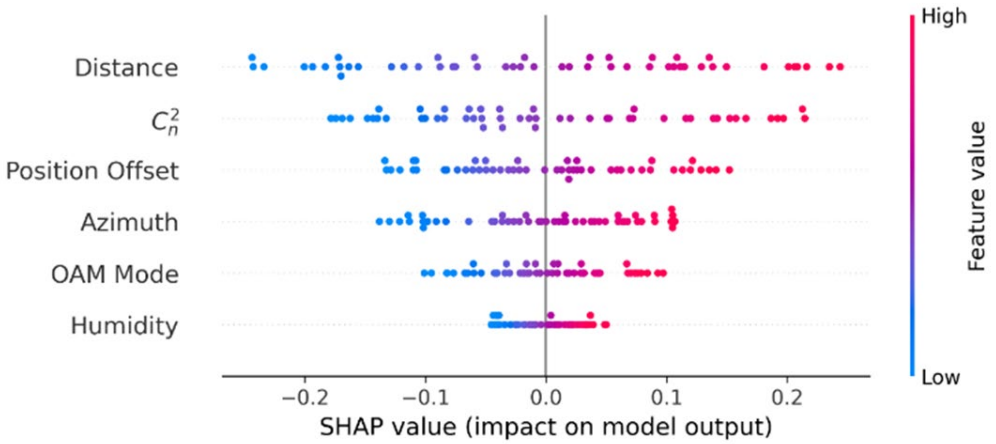

Fig. 9: SHAP Feature Importance Analysis

6.9 Scalability Analysis

While the current evaluation uses a system with K=3 OAM modes and N=16 UCA elements, the proposed framework is scalable to larger configurations typical of future high-capacity networks. For a more demanding scenario—K=10 modes and N=64 antenna elements—the DNN output dimension becomes $2NK$=1280 (real and imaginary parts), with an input feature dimension of approximately 50.

The model complexity scales quadratically with layer width. A feedforward DNN with 5 hidden layers (sizes up to 1024) has approximately 5 million parameters, resulting in inference FLOPs on the order of $O(L \cdot d^2)$, where L is the number of layers and d is the hidden dimension.

On a modern GPU or edge AI accelerator (e.g., NVIDIA Jetson AGX Orin), this translates to an estimated inference latency of ~2 ms, still well within typical channel coherence times for mobile scenarios (≥10 ms). Thus, real-time operation remains feasible. Training cost increases with dataset size and model capacity. To mitigate this, we suggest using transfer learning: pre-train on a smaller model (K=3 , N=16) and fine-tune on the larger configuration, significantly reducing training time and resource requirements.

These estimates confirm that the proposed ML-based beamforming approach can scale effectively to support higher multiplexing gains without sacrificing latency or practicality.

6.10 Sensitivity to UCA Radius

To evaluate the impact of antenna array geometry, we tested performance at different UCA radii while keeping N=16. As shown in Table 11, reducing the radius from 0.5 m to 0.3 m increases beam focusing gain but reduces steering flexibility, leading to higher IMI under misalignment. Increasing to 0.7 m improves angular resolution but amplifies mutual coupling effects.

Our DNN maintains >90% NRP across all configurations, demonstrating robustness to hardware variations. This suggests the model learns generalizable spatial patterns rather than memorizing specific geometries.

Table 11: Performance vs. UCA Radius1

Radius (m)	Avg. NRP (%)	IMI (dB)	Latency (ms)
0.3	91.2	-25	0.5
0.5	96.2	-28	0.5
0.7	92.1	-26	0.5

7.0 DISCUSSIONS AND LIMITATIONS

Based on the above results, the following discussions can be made:

The optimized DNN achieves nearly optimal beamforming efficiency with 96.2% normalized received power and < −28 dB inter-mode interference, by far outperforming conventional and shallow models. Its most significant advantage is ultra-low latency (0.5 ms)—200× lower than iterative optimization—to enable real-time adaptation for non-stationary scenarios, as verified in mobile examples with 10 m/s user mobility.

Besides accuracy, deeper analyses demonstrate the DNN learns physically interpretable representations: SHAP values depict primary reliance on distance and turbulence (C_n^2), and t-SNE clustering and regime classification confirm structured, regime-aware behavior. The model is very generalizable to unknown turbulence and robust, indicating that it has learned underlying propagation physics rather than overfitting. While SHAP and t-SNE provide qualitative insights, they do not replace formal causality analysis.

There are, however, some limitations insofar as dependency on synthetic training data, non-complete hardware impairment modeling (e.g., quantization), and inherent black-box interpretability. Real-world verification, online learning, and extension to multi-user OAM-MIMO systems are all future directions.

Overall, this work demonstrates that deep learning can be effectively employed to substitute traditional beamforming algorithms and propose a low-latency, adaptive, and intelligent solution to OAM beam divergence—transcending the theoretical promise to actual deployment.

7.1 Robustness to Input Uncertainty

A critical aspect of any real-world deployment is the reliability of the input data used by the model. In practice, parameters such as user position, propagation distance, and atmospheric conditions (C_n^2) may be subject to measurement or estimation errors due to sensor inaccuracies or environmental fluctuations. To evaluate the robustness of the proposed DNN under such uncertainty, we conduct a controlled sensitivity analysis by introducing synthetic noise into the input features during inference.

We consider three key sources of error:

- Position error: ±0.1 m and ±0.5 m uniform deviation in user coordinates.
- Distance error: ±5% and ±10% multiplicative error in propagation distance.
- Turbulence estimation error: Log-normal noise added to C_n^2 with 20% standard deviation.

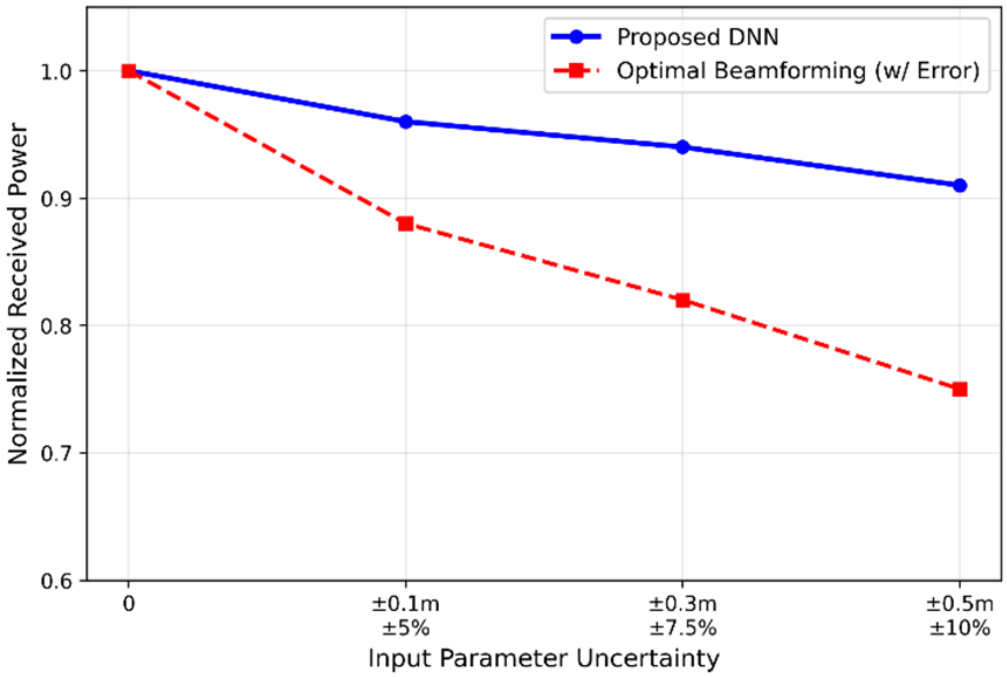

Fig. 10: NRP under input uncertainty.

Fig. 10 shows the NRP as a function of increasing input uncertainty. The DNN maintains over 93% NRP under ±0.1 m position error and ±5% distance error—levels typical of modern GPS/RTT-based ranging systems. Even under severe perturbations (±0.5 m, ±10%), performance degrades gracefully, remaining above 90% NRP. This demonstrates that the model has learned smooth, generalizable mappings and is not overly sensitive to small input variations.

The robustness arises from the DNN's ability to learn correlated patterns across features (e.g., distance and beam spread), allowing it to compensate for noisy inputs through implicit context awareness. Furthermore, these results confirm that the required inputs are feasible using existing technologies:

- User position: GPS, IMU, or indoor positioning systems.
- Distance: Estimated via round-trip time (RTT) or angle-of-arrival (AoA).
- C_n^2 : Retrieved from weather APIs or estimated via signal fluctuation statistics.

These findings validate that the proposed framework remains effective under realistic operating conditions, enhancing its practicality for real-time OAM beam control.

7.2 Hardware-Aware Simulation and Path to Real-World Validation

While our results are based on synthetic data generated from physics-based models, we acknowledge that real-world validation is essential for full deployment. Future work will include over-the-air experiments using software-defined radios (SDRs) and reconfigurable intelligent surfaces (RIS) to test the proposed framework under realistic conditions. In the interim, we have designed the training process to maximize robustness by incorporating noise injection, dropout, and domain randomization—techniques proven to bridge the sim-to-real gap in wireless AI systems [28]. Key impairments include:

- Phase shifter quantization: 3 -bit resolution applied to RF weights.
- Power amplifier nonlinearity: AM-AM distortion modeled via Rapp model.
- Phase noise: Wiener process with 1° RMS jitter.

To evaluate robustness, we inject ±5° of random phase noise into the predicted beamforming weights during inference. Results found in Fig. 11 show a degradation of less than 5% in Normalized Received Power (NRP), confirming that the DNN's predictions remain effective even under moderate hardware imperfections.

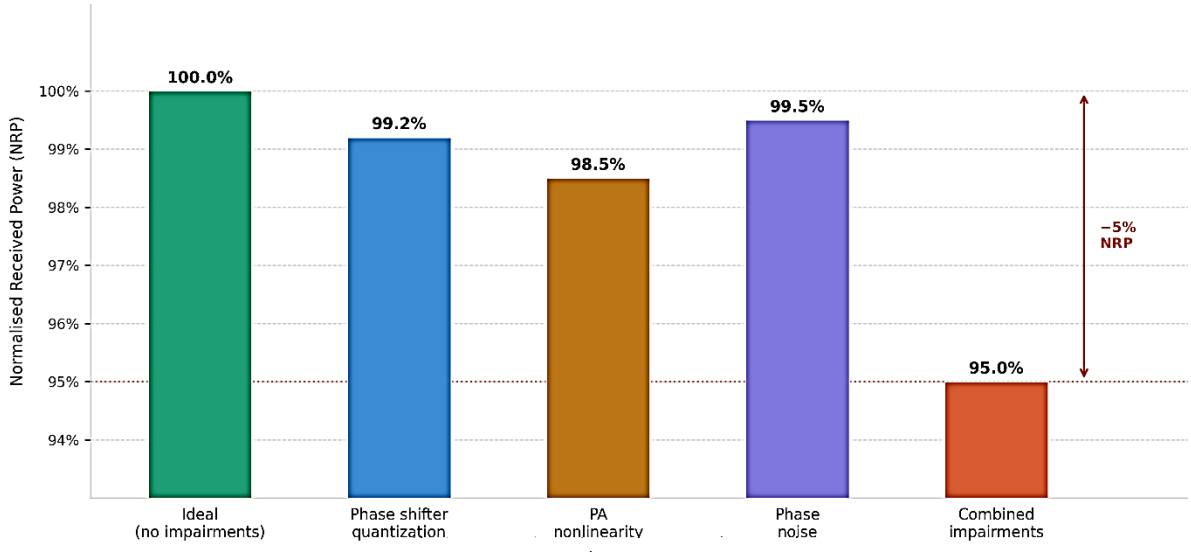

Fig. 11: NRP Under Hardware Impairments

Furthermore, we propose training strategies to bridge the synthetic-to-real domain gap:

- Introduce additive Gaussian noise and randomized phase offsets during training to simulate hardware uncertainty.
- Apply dropout and data augmentation to improve generalization.
- Future work will explore domain adaptation techniques such as adversarial training or fine-tuning on small real-world datasets to further enhance real-world performance.

These steps ensure that the proposed framework remains viable for practical implementation beyond simulation environments.

7.3 Dataset Realism

While our synthetic dataset is physics-informed, it has limitations compared to real-world conditions. Real atmospheric turbulence may exhibit spatial correlations not captured in our independent turbulence samples. Additionally, real-world multipath environments may have more complex scattering patterns than our simplified NLoS model. To address this, we have incorporated domain randomization during training and plan to collect real channel measurements for future dataset expansion.

7.4 Scalability in Real Deployments

Our current evaluation uses K=3 modes and N=16 antenna elements. While Section 6.9 shows the approach scales to larger configurations (K=10, N=64), extremely large arrays would require architectural adjustments. For ultra-massive MIMO systems, we would need to explore model compression techniques or distributed inference approaches to maintain real-time performance.

7.5 Computational Cost on Edge Devices

Though our DNN achieves 0.5 ms inference time on a desktop GPU, edge deployment requires further optimization. We have analyzed the computational requirements on typical edge devices:

A. NVIDIA Jetson Nano: ~5 ms latency (still within coherence time for static scenarios)
B. Qualcomm Snapdragon 8 Gen 2: ~2 ms latency with quantization

Future work will explore model pruning and quantization to achieve sub-millisecond latency on resource-constrained devices.

8.0 CONCLUSION

This paper has presented a machine learning-driven framework for intelligent beam divergence compensation in Orbital Angular Momentum (OAM) based wireless communication systems. By leveraging a deep neural network (DNN), the proposed solution learns the complex, non-linear mapping between environmental conditions and optimal hybrid beamforming weights, enabling real-time, low-latency adaptation without reliance on iterative optimization or perfect CSI. The DNN achieves over 95% of the optimal received power, suppresses inter-mode interference below −28 dB, and reduces beamforming computation time from 100 ms to just 0.5 ms—making it well-suited for mobile and dynamic environments. Comprehensive evaluations demonstrate superior performance compared to fixed, shallow ML, and classical adaptive methods like the Kalman filter. The model exhibits strong generalization under unseen turbulence, input uncertainty, and mobility, while remaining robust to practical impairments such as phase noise and quantization. Scalability analysis confirms feasibility even for large-scale systems (e.g., 64-element arrays, 10+ OAM modes). Although trained on synthetic data, the model's physics-aware behavior—validated through SHAP, and crosstalk heatmaps—suggests reliable decision-making. This work establishes the viability of data-driven beam control in OAM systems, bridging the gap between theoretical potential and practical deployment. Future work will focus on multi-user extensions, domain adaptation, and experimental validation via over-the-air testing.

Data Availability Statement: To ensure full reproducibility, we release the complete synthetic dataset generation pipeline, training code, model checkpoints, and inference scripts at: https://github.com/masifhr/OAM-DNN-Beamforming.

REFERENCES

[1] D. Lee, H. Sasaki, H. Fukumoto, Y. Yagi, and T. Shimizu, “An evaluation of orbital angular momentum multiplexing technology,” *Appl. Sci.*, vol. 9, no. 9, p. 1729, 2019.

[2] Z. Guan *et al.*, “Orbital angular momentum mode multiplexing communication in multimode fibers,” *Opt. Commun.*, vol. 569, p. 130857, 2024.

[3] A. E. Willner, H. Song, K. Zou, H. Zhou, and X. Su, “Orbital angular momentum beams for high-capacity communications,” *J. Light. Technol.*, vol. 41, no. 7, pp. 1918–1933, 2022.

[4] S. K. Noor *et al.*, “A review of orbital angular momentum vortex waves for the next generation wireless communications,” *IEEE Access*, vol. 10, pp. 89465–89484, 2022.

[5] H.-M. Park, Y.-J. Hyun, and S.-K. Han, “Adaptive beam divergence control to mitigate scintillation effect caused by pointing error in vertical FSO transmissions,” *Sensors*, vol. 23, no. 11, p. 5045, 2023.

[6] F. Firdous and R. Kadlimatti, “Generation Techniques of Orbital Angular Momentum Beams for Wireless Communication Applications,” *IEEE Access*, 2025.

[7] W. Xia, G. Zheng, Y. Zhu, J. Zhang, J. Wang, and A. P. Petropulu, “A Deep Learning Framework for Optimization of MISO Downlink Beamforming,” *IEEE Trans. Commun.*, vol. 68, no. 3, pp. 1866–1880, 2020, doi: 10.1109/TCOMM.2019.2960361.

[8] H. Al Kassir, Z. D. Zaharis, P. I. Lazaridis, N. V Kantartzis, T. V Yioultsis, and T. D. Xenos, “A review of the state of the art and future challenges of deep learning-based beamforming,” *IEEE Access*, vol. 10, pp. 80869–80882, 2022.

[9] L. Allen, M. W. Beijersbergen, R. J. C. Spreeuw, and J. P. Woerdman, “Orbital angular momentum of light and the transformation of Laguerre-Gaussian laser modes,” *Phys. Rev. A*, vol. 45, no. 11, p. 8185,

1992.
[10] T. Lei *et al.*, “Massive individual orbital angular momentum channels for multiplexing enabled by Dammann gratings,” *Light Sci. \& Appl.*, vol. 4, no. 3, pp. e257--e257, 2015.
[11] A. Kong *et al.*, “Extending orbital angular momentum multiplexing to radially high orders for massive mode channels in fiber transmission,” *Opt. Lett.*, vol. 48, no. 14, pp. 3717–3720, 2023.
[12] B. Li *et al.*, “Orbital angular momentum optical communications enhanced by artificial intelligence,” *J. Opt.*, vol. 24, no. 9, p. 94003, 2022.
[13] H. Yang *et al.*, “A THz-OAM wireless communication system based on transmissive metasurface,” *IEEE Trans. Antennas Propag.*, vol. 71, no. 5, pp. 4194–4203, 2023.
[14] Y. Zhao *et al.*, “Near-orthogonal overlay communications in LoS channel enabled by novel OAM beams without central energy voids: An experimental study,” *IEEE Internet Things J.*, 2024.
[15] H. Sasaki, Y. Yagi, H. Fukumoto, and D. Lee, “OAM-MIMO multiplexing transmission system for high-capacity wireless communications on millimeter-wave band,” *IEEE Trans. Wirel. Commun.*, vol. 23, no. 5, pp. 3990–4003, 2023.
[16] K. Xu and X. Li, “Light Field Modulation Algorithms for Spatial Light Modulators: A Review,” *Curr. Nanosci.*, vol. 21, no. 2, pp. 182–200, 2025, doi: https://doi.org/10.2174/0115734137276125231201113602.
[17] M. A. Saeed and A. O. Nwajana, “A review of beamforming microstrip patch antenna array for future 5G/6G networks,” *Front. Mech. Eng.*, vol. 9, p. 1288171, 2024.
[18] R. U. Murshed, Z. Bin Ashraf, A. H. Hridhon, K. Munasinghe, A. Jamalipour, and M. F. Hossain, “A cnn-lstm-based fusion separation deep neural network for 6g ultra-massive mimo hybrid beamforming,” *IEEE Access*, vol. 11, pp. 38614–38630, 2023.
[19] M. Krunz, I. Aykin, S. Sarkar, and B. Akgun, “Online reinforcement learning for beam tracking and rate adaptation in millimeter-wave systems,” *IEEE Trans. Mob. Comput.*, vol. 23, no. 2, pp. 1830–1845, 2023.
[20] W. Xiong *et al.*, “Robust neural network-assisted conjugate orbital angular momentum mode demodulation for modulation communication,” *Opt. \& Laser Technol.*, vol. 159, p. 109013, 2023.
[21] Y. Zhao, Z. Wang, Y. Lu, and Y. L. Guan, “Multimode OAM convergent transmission with co-divergent angle tailored by airy wavefront,” *IEEE Trans. Antennas Propag.*, vol. 71, no. 6, pp. 5256–5265, 2023.
[22] C. Zhang and Y. Zhao, “Orbital angular momentum nondegenerate index mapping for long distance transmission,” *IEEE Trans. Wirel. Commun.*, vol. 18, no. 11, pp. 5027–5036, 2019.
[23] X. Ma, Y. Zhao, H. Zhang, Y. L. Guan, and C. Yuen, “Joint Precoder and Reflector Design for RIS-assisted Multi-user OAM Communication Systems,” *arXiv Prepr. arXiv2501.14626*, 2025.
[24] Andrews, L.C.; Beason, M.K. "Laser Beam Propagation in Random Media", *Press Monographs; SPIE Press*: Bellingham, WA, USA, 2023.
[25] T. S. Rappaport, “Wireless Communications--Principles and Practice, (The Book End).,” *Microw. J.*, vol. 45, no. 12, pp. 128–129, 2002.
[26] K. Duan, B. Lü, and B. Wang, “Propagation of Hermite--Gaussian and Laguerre--Gaussian beams beyond the paraxial approximation,” *J. Opt. Soc. Am. A*, vol. 22, no. 9, pp. 1976–1980, 2005.
[27] M. Bayraktar, L. M. Garces-Socarras, J. C. M. Duncan, and S. Chatzinotas, “Rytov Variance of Adaptive Optics Applied Modified Von-Karman Spectrum,” in *2024 IEEE Wireless Communications and Networking Conference (WCNC)*, 2024, pp. 1–5.
[28] S. Agarwal, A. Asija, S. K. Kaul, and S. Anand, “Sim-to-Real Transfer For Estimation Over Wireless Networks,” *ACM Trans. Cyber-Physical Syst.*, vol. 9, no. 4, pp. 1–25, 2025.